Inorganic Chemistry
Cite This: Inorg. Chem. XXXX, XXX, XXX–XXX
Article
pubs.acs.org/IC

A Tetraphenylethene Luminogen-Functionalized Gemini Surfactant for Simple and Controllable Fabrication of Hollow Mesoporous Silica Nanorods with Enhanced Fluorescence

Saisai Yan,[†,‡] Zhinong Gao,*[,†,‡] Yan Xia,[†,‡] Xueming Liao,[†,‡] Yifan Chen,[§] Jia Han,[†,‡] Chenchen Pan,[†,‡] and Yingfang Zhang[†,‡]

[†]College of Chemistry and Molecular Sciences, Wuhan University, Wuhan, Hubei 430072, P. R. China
[‡]Key Laboratory of Biomedical Polymers, Ministry of Education of China, Wuhan, Hubei 430072, P. R. China
[§]School of Materials Science and Chemistry Engineering, China University of Geosciences, Wuhan, Hubei 430074, P. R. China

Supporting Information

ABSTRACT: Nanoparticles that possess unique structures and properties are highly desired in the production of multifunctional materials because of their combinational performance. In this study, a facile and effective fabricating strategy is developed to controllably prepare fluorescent hollow mesoporous silica nanorods via the cetyltrimethylammonium bromide (CTAB) and tetraphenylethene (TPE) luminogen-functionalized gemini surfactant (C_{TPE}–C_6–C_{TPE}) guided dual-templating approach. Because of its unique chemical structure, water solubility, surface activity, and fluorescent properties, the designed C_{TPE}–C_6–C_{TPE} will not only provide an anchored fluorophore for silica nanoparticles but also serve as an intimate partner of CTAB to regulate their construction in the structure-directing process. By properly tuning the molar ratio of CTAB/C_{TPE}–C_6–C_{TPE}, the shape-controlled aggregation-induced emission hollow mesoporous silica nanoparticles (AIE-MSNs) can be prepared directly, producing two kinds of silica nanorods (AIE-MSNs-15 and AIE-MSNs-7). In particular, the incorporated bulky TPE luminogens will not only endow AIE-MSNs-7 with enhanced fluorescence intensity (2.3-fold) after the removal of CTAB but also bring about high accessible surface area (606.6 m^2/g) and larger pore size (3.2 nm) and pore volume (0.634 cm^3/g) for effective loading and sustained release of the hydrophobic anticancer drug camptothecin. C_{TPE}–C_6–C_{TPE} enriches the family of gemini surfactants and provides important insights into the convenient fabrication of advanced fluorescent mesoporous materials.

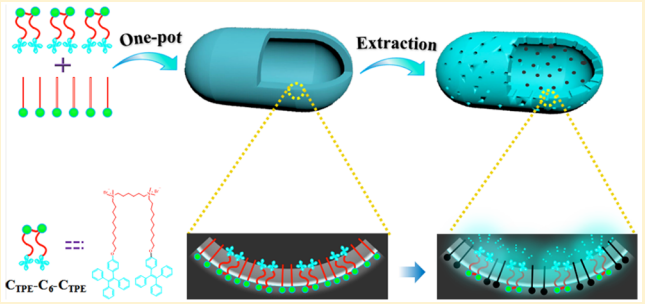

1. INTRODUCTION

Multifunctional nanoplatforms, which integrate various functional components into a single system, have been in the spotlight of producing theranostic nanomedicines for early diagnosis and therapies of cancer.[1] Remarkable achievements have been made in the design and fabrication of various nanoplatforms such as polymers, liposomes, dendrimers, nanogels, and other hybrid nanomaterials.[1−3] Among the various materials that have been proposed for preparing smart nanoplatforms, silica nanoparticles (SNs) are among the most promising candidates for the integration of designated modalities and functionalities by virtue of their intrinsically attractive properties including rigid structure, ideal chemical stability, tunable pore structure, ease of surface functionalization, and good biocompatibility.[4−7] As a well-developed nanoplatform, mesoporous SNs (MSNs) have numerous advantages that include stable structures, abundant mesopores, high specific surface areas, and large pore volumes.[8−10] The incorporation of anticancer drugs, targeting molecules, and stimuli-responsive elements with MSNs enables guided delivery and release in targeted cells.[11] With advances in synthetic nanoscience and nanotechnology, hollow MSNs have been proposed to optimize the structure of SNs and expand their application areas.[12−14] The well-defined hollow MSNs can provide both capacious interiors and intact porous shells, affording high storage/adsorption capacity and accessible mesoporous channels for mass transfer and diffusion, which are beneficial for sustained-release behavior and synergistic effects with guest molecules.[15−18] The controllable MSNs with hollow or rattle structure are considered to be ideal drug-delivery vehicles, offering additional possibilities for the tailoring of material properties toward a broad range of applications.[19,20]

The recently emerged aggregation-induced emission fluorogens (AIEgens) have sparked increasing research interest in biosensing and imaging because of their unique advantages such as low background interference, a high signal-to-noise

Received: August 8, 2018

DOI: 10.1021/acs.inorgchem.8b02252
Inorg. Chem. XXXX, XXX, XXX–XXX

Scheme 1. (a) Synthetic Route of the TPE-Functionalized Gemini Surfactant C_{TPE}–C_6–C_{TPE} (4) and (b) Schematic Illustration of the Main Procedures in the Fabrication of AIE-MSNs

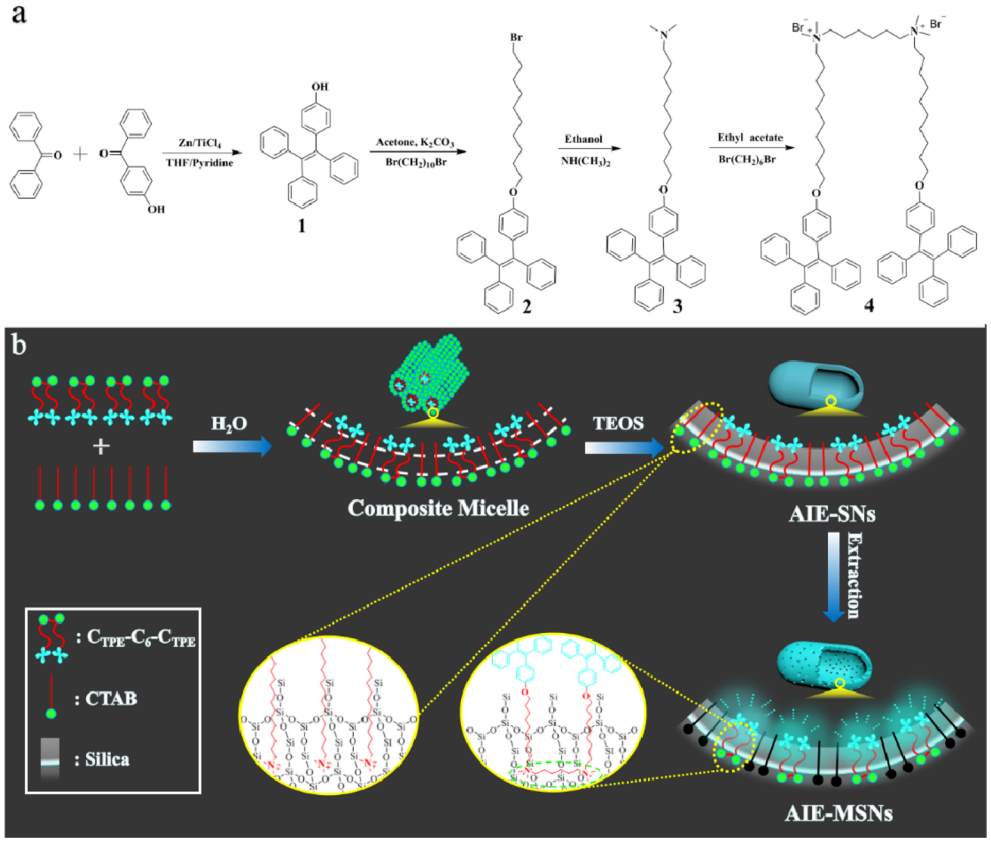

ratio, and superior photostability with activatable therapeutic effects.[21] Compared with conventional fluorophores, the AIE effect offers a timely remedy to tackle the challenge of notorious aggregation-caused quenching (ACQ) and provides new degrees of freedom for real-time, on-site, and noninvasive visualization.[22−24] With regard to the construction of multifunctional nanoplatforms and ultimately advanced materials, great efforts have recently been made to integrate AIEgens with silica moieties into one nanostructure so as to develop a new family of functional composite nanomaterials for sensitive optical sensing and efficient therapy.[22,25] Physical blending is a simple and facile synthetic approach to generating AIEgens-functionalized SNs (AIE-SNs) by doping AIE molecules within the silica matrix.[5] Wei and co-workers have made the first attempt to integrate cell imaging with cancer therapy in one AIE-MSNs system via the one-pot coassembly of cetyltrimethylammonium bromide (CTAB), a silica source, and hydrophobic AIE molecules.[4] Undesirably, leakage of the dopants from the AIE-MSNs may happen because of weak interactions between the organic and inorganic phases, resulting in the inevitable decrease of the fluorescence intensity. Besides, the reported literatures involved only the preparation of ordinary nonhollow spherical AIE-MSNs or AIE-SNs because of the lack of effective directing in the sol–gel process. The chemical-bonded hollow AIE-MSNs have also been developed to overcome the above-mentioned drawbacks.[25,26] However, their preparation procedures are rather complex and mainly rely on multistep improvement based on the existing nanostructure, which is not favorable in large-scale applications. It is urgent to overcome these limitations and develop a new straightforward method for the facile and controllable preparation of hollow AIE-MSNs.

Surfactants play a critical role in controlling the morphology, pore size, surface area, and dimension when preparing SNs by a template-directed method.[27−29] Among the various surfactants currently available, gemini surfactants, as a new class of surfactants containing one unique structure of two amphiphilic moieties connected with a spacer, have always been considered to be promising stabilizers and structure director agents for the preparation of various nanomaterials because of their better interfacial properties, miscellaneous aggregate morphologies, charged head groups, and lower critical micelle concentrations (CMCs).[30−32] In our previous work, the improved gemini surfactant C_{16}–TPE–C_{16} with a tetraphenylethene (TPE) luminogen-functionalized spacer, together with conventional CTAB, was successfully employed to prepare hollow AIE-MSNs.[33] Although the obtained hollow AIE-MSNs exhibit less uniform morphologies, small mesopores of 2.8 nm, and unfavorable weakening of the fluorescent intensity after the removal of CTAB, they inspired us to pursue more suitable gemini surfactants to improve their structures and properties.

Herein, we designed and synthesized a new TPE-functionalized gemini surfactant (Scheme 1a, denoted as C_{TPE}–C_6–C_{TPE}) to serve as an intimate partner of CTAB for the simple and controllable fabrication of hollow AIE-MSNs. The TPE luminogens connecting at the tails endowed C_{TPE}–C_6–C_{TPE} with unique surface activity, stability, sensitivity, and AIE effect, bringing about simultaneous photoluminescence in the dispersed, aggregated, and solid states. With the help of C_{TPE}–C_6–C_{TPE} and CTAB, a facile and effective bottom-up coassembled strategy is developed to controllably prepare

DOI: 10.1021/acs.inorgchem.8b02252
Inorg. Chem. XXXX, XXX, XXX−XXX

AIE-SNs in H_2O, followed by an extraction process to generate AIE-MSNs with abundant mesoporous and enhanced fluorescence (Scheme 1b). The designed $C_{TPE}-C_6-C_{TPE}$ will not only provide an anchored fluorophore for AIE-SNs and AIE-MSNs but also cooperate with CTAB to regulate their construction as structure-directing agents. By proper tuning of the molar ratio of CTAB/$C_{TPE}-C_6-C_{TPE}$, the shape-controlled AIE-MSNs with improved structures and fluorescent properties can be prepared directly. Additionally, the delivery of the hydrophobic anticancer drug camptothecin (CPT) was further performed to evaluate the drug loading and release behavior of the resultant hollow AIE-MSNs.

2. EXPERIMENTAL SECTION

2.1. Materials and Instruments. Zinc dust, benzophenone, 4-hydroxybezophenone, 1,10-dibromodecane, 1,6-dibromohexane, dimethylamine (33%), and camptothecin (CPT) were purchased from Aladdin. $TiCl_4$, K_2CO_3, NaOH, CH_2Cl_2, Na_2SO_4, ethanol, methanol, acetone, pyridine, ethyl acetate, petroleum ether, tetrahydrofuran (THF), hydrochloric acid (HCl), tetraethylorthosilicate (TEOS), and cetyltrimethylammonium bromide (CTAB) were purchased from Sinopharm Chemical Reagent Co. All reagents were of analytical grade and were used without further purification. H_2O was purified by a Milli-Q system (Millipore, Molsheim, France) and used in all of the experiments.

IR spectra were recorded in the range of 4000−400 cm^{-1} using KBr pellets on a Thermo Nicolet 5700 spectrophotometer. ^1H and ^{13}C NMR were obtained from a Bruker Ascend-400 MHz spectrometer using $CDCl_3$ or dimethyl sulfoxide (DMSO)-d_6 as a solvent. Electrospray ionization mass spectrometry (ESI-MS) spectra were recorded on a LCQ spectrometer (Finnigan, USA). UV−vis spectra were measured on a Shimadzu UV-2600 spectrophotometer. Fluorescence spectra were obtained on a RF-5301PC fluorescence spectrometer (Shimadzu, Japan) with the slit of 3.0 nm. The field-emission scanning electron microscopy (FESEM) was performed on a Zeiss Sigma field-emission scanning electron microscope (20 kV). Transmission electron microscopy (TEM) images were recorded on a JEM-2100 microscope (200 kV). The surface tension values were measured following the Wilhelmy plate procedure at 25.0 °C with a QBZY-2 tensiometer (Fangrui Corp., China). Electrical conductivity was performed at 25.0 °C with a WTW conductivity meter (inoLab Cond730, Germany). The nitrogen adsorption−desorption isotherms were carried out on a Micromeritics ASAP 2020 system (USA) at 77 K. The Brunauer−Emmett−Teller (BET) method was conducted to calculate the specific surface areas. The Barrett−Joyner−Halenda model was utilized to calculate the pore-size distributions from the desorption branches of the isotherms.

2.2. Preparation of the $C_{TPE}-C_6-C_{TPE}$. The TPE-functionalized gemini surfactant $C_{TPE}-C_6-C_{TPE}$ was synthesized according to the procedures described in Scheme 1a.

(i) The synthesis of compound **1** was performed by the powerful McMurry reaction as reported previously.[23] Yield: 61%. ^1H NMR (400 MHz, DMSO-d_6): δ 9.38 (s, 1 H), 7.16−7.04 (m, 9 H), 6.92−6.98 (m, 6 H), 6.72−6.75 (d, 2 H), 6.49−6.52 (d, 2 H).

(ii) Synthesis of compound **2**: Compound **1** (0.0560 g, 0.16 mmol) and K_2CO_3 (0.066 g, 0.48 mmol) were mixed in acetone (20 mL). Then, 1,10-dibromodecane (0.096 g, 0.32 mmol) was added dropwise after stirring for 30 min. The resulting mixture was refluxed for 8 h [monitored by thin-layer chromatography (TLC)] and cooled to room temperature. After filtration of insoluble K_2CO_3 and vacuum distillation, the crude product was purified by silica gel chromatography with petroleum ether/ethyl acetate [20:1 (v/v)] as the eluent. The final product was obtained as a yellowish oil. Yield: 76%. ^1H NMR (400 MHz, $CDCl_3$): δ 6.99−7.14 (m, 15 H), 6.89−6.93 (m, 2 H), 6.59−6.64 (m, 2 H), 3.86 (t, 2 H), 3.41 (t, 2 H), 1.89 (m, 2 H), 1.72 (m, 2 H), 1.30−1.42 (m, 12 H). ^{13}C NMR (400 MHz, $CDCl_3$): δ 157.70, 144.05, 140.61, 139.98, 135.90, 132.55, 131.45, 127.62, 126.24, 113.56, 67.78, 34.15, 32.86, 29.49, 29.47, 29.41, 29.34, 28.80, 28.21, 26.09.

(iii) Synthesis of compound **3**: Compound **2** (0.30 g, 0.53 mmol) and K_2CO_3 (0.073 g, 0.53 mmol) were added to a 50 mL round-bottom flask with ethanol (20 mL). Then, dimethylamine (0.048 g, 1.06 mmol) was added slowly to this solution. After that, the reaction mixture was heated with refluxing for 15 h (monitored by TLC) and cooled to room temperature. The solution was concentrated, the residue was poured into a NaOH aqueous solution (20 mL, 1 M), and the product was taken up with ethyl acetate. The organic layer was collected and dried with anhydrous Na_2SO_4. The crude product was purified by column chromatography with ethyl acetate/methanol [15:1 (v/v)] as the eluent to obtain the target compound (yellow oil). Yield: 90%. ^1H NMR (400 MHz, $CDCl_3$): δ 6.99−7.14 (m, 15 H), 6.89−6.93 (m, 2 H), 6.60−6.64 (m, 2 H), 3.86 (t, 2 H), 3.24 (m, 2 H), 3.18 (s, 6 H), 1.86 (m, 2 H), 1.73 (m, 2 H), 1.30−1.43 (m, 12 H). ^{13}C NMR (400 MHz, $CDCl_3$): δ 157.59, 143.98, 140.51, 139.91, 135.84, 132.47, 131.33, 127.55, 126.17, 113.48, 71.65, 67.71, 58.32, 55.38, 29.37, 29.31, 29.28, 29.26, 26.60, 26.01, 23.89.

(iv) Synthesis of $C_{TPE}-C_6-C_{TPE}$ (compound **4**): Compound **3** (0.90 g, 1.69 mmol) and 1,6-dibromohexane (0.17 g, 0.70 mmol) were dissolved in ethyl acetate (20 mL). Then, the reaction was allowed to stir and reflux for 4 days. After the reaction cooled to room temperature, the resulting mixture was filtered to obtain a white precipitate (crude product). The collected product was further washed with ethyl acetate and recrystallized from ethyl acetate/ethanol at least three times to get the purified product as a white solid. Yield: 68%. ^1H NMR (400 MHz, $CDCl_3$): δ 6.97−7.09 (m, 30 H), 6.86−6.91 (m, 4 H), 6.57−6.62 (m, 4 H), 3.83 (t, 4 H), 3.69 (m, 4 H), 3.47 (m, 4 H), 3.36 (s, 12 H), 1.98 (m, 4 H), 1.70 (m, 8 H), 1.27−1.40 (m, 28 H). ^{13}C NMR (400 MHz, $CDCl_3$): δ 157.58, 143.96, 140.50, 139.90, 135.81, 132.46, 131.29, 127.54, 126.17, 113.48, 67.69, 64.63, 64.05, 50.97, 29.37, 29.33, 29.29, 29.27, 29.25, 26.28, 26.02, 24.45, 22.85, 21.65. IR (KBr, cm^{-1}): 3021 (m), 2925 (vs), 2854 (s), 1604 (s), 1508 (vs), 1470 (s), 1393 (m), 1244 (vs), 1176 (s), 1029 (m), 809 (w), 730 (m), 701 (vs). UV−vis: λ_{max} = 319 nm. ESI-MS (CH_3OH, m/z): $[M - Br]^+$, calcd 1227.6, found 1227.5; $[M - 2Br]^{2+}/2$, calcd 573.9, found 573.9.

2.3. Preparation of the AIE-MSNs, CTAB-MSNs, MSNs-15, and MSNs-7. AIE-MSNs were prepared by two steps according to our previous report.[33] Briefly, CTAB and $C_{TPE}-C_6-C_{TPE}$ with a total amount of 0.137 mmol were first dissolved in ultrapure H_2O (25 mL). The molar ratio of CTAB and $C_{TPE}-C_6-C_{TPE}$ was as follows: CTAB:$C_{TPE}-C_6-C_{TPE}$ = n:1 (n = 40, 35, 30, 25, 20, 15, 10, 7, and 5). Then, the aqueous solution of NaOH (0.180 mL, 2.00 M) was introduced into the mixed solution. The temperature of the mixture was adjusted to 80 °C and kept for 30 min. Subsequently, TEOS (0.50 mL, 2.24 mmol) was added dropwise under vigorous stirring. The mixture was allowed to react for 4 h to give a white precipitate. The obtained product was collected by centrifugation and washed with H_2O and ethanol several times to yield AIE-SNs. Finally, the synthesized AIE-SNs (0.5 g) were refluxed in a solution of ethanol (50.0 mL) and HCl (3.0 mL, 37.4%) for 24 h to remove CTAB. The obtained product was collected by centrifugation, washed with H_2O and ethanol, and dried at 35 °C in a vacuum to yield the AIE-MSNs. Additionally, the preparation of comparing CTAB-SNs and CTAB-MSNs was performed with the individual CTAB under the same procedure as that described above.

The surfactant template in SNs can be completely removed by the calcination treatment.[14] In order to calcine out the encapsulated $C_{TPE}-C_6-C_{TPE}$ component in AIE-SNs, the obtained AIE-MSNs-15 and AIE-MSNs-7 were further subjected to thermal treatment at 600 °C for 8 h in air, and the corresponding products were designated as MSNs-15 and MSNs-7, respectively.

2.4. In Vitro Drug Loading and Release. To evaluate the drug loading capacity of AIE-MSNs, CPT was used as a model guest molecule in the experiment and the process was performed according to the reported literature.[9] Briefly, 40 mg each of AIE-MSNs (AIE-MSNs-15 or AIE-MSNs-7) and MSNs (MSNs-15 or MSNs-7) were respectively dispersed in the solution of CPT (5 mL, 5 mg/mL) in

DOI: 10.1021/acs.inorgchem.8b02252
Inorg. Chem. XXXX, XXX, XXX−XXX

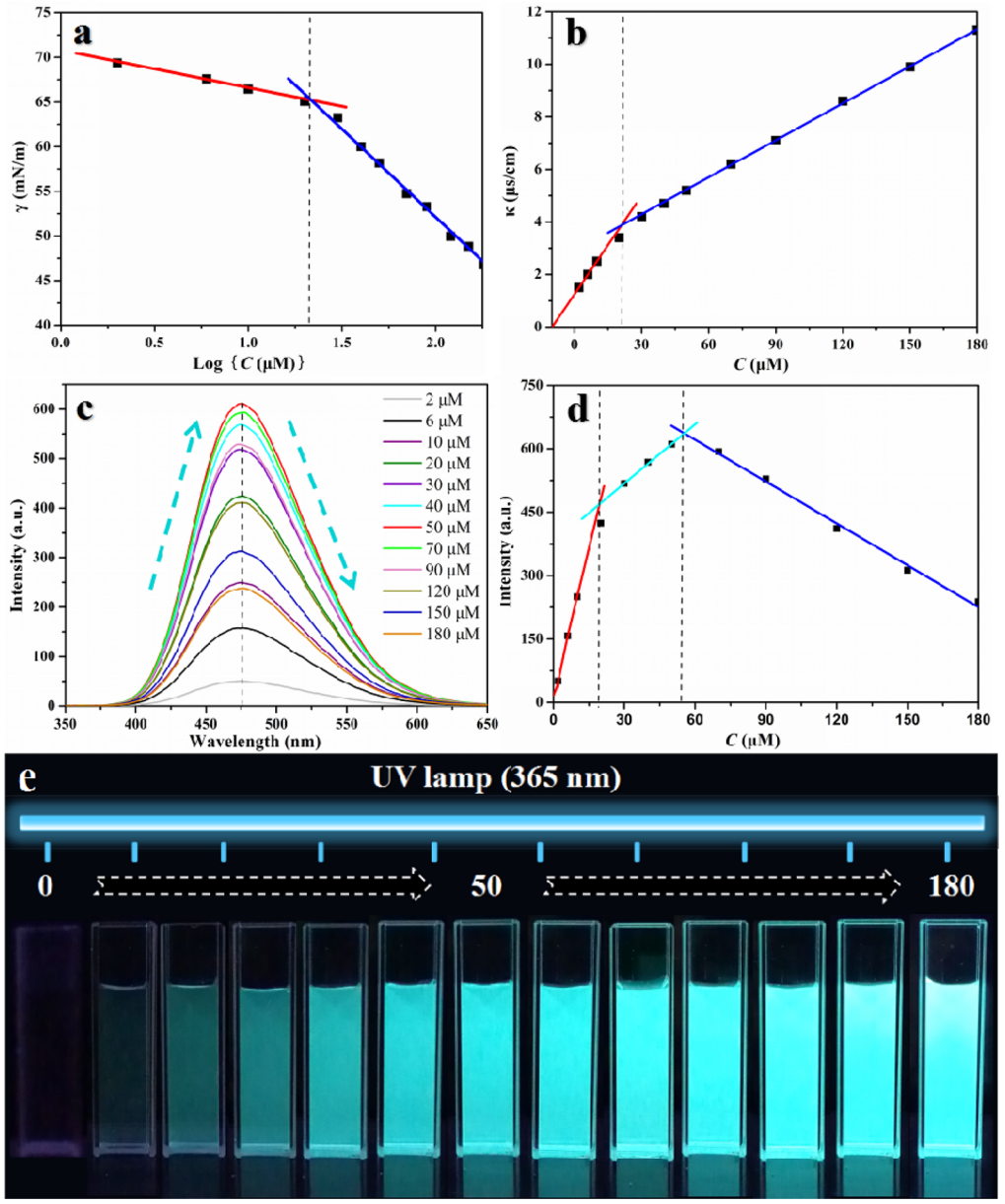

Figure 1. (a) Plot of the surface tension (γ) versus log(C) for C_{TPE}–C_6–C_{TPE}. (b) Plot of the conductivity (κ) versus the concentration of C_{TPE}–C_6–C_{TPE}. (c) Fluorescence spectra of C_{TPE}–C_6–C_{TPE} in aqueous solution with the concentration increased from 2 to 180 μM (λ_{ex} = 340 nm). (d) Plot of the fluorescence intensity of C_{TPE}–C_6–C_{TPE} at 475 nm versus the corresponding concentration in part c. (e) Fluorescence photographs of C_{TPE}–C_6–C_{TPE} in aqueous solution at concentrations from 0 to 180 μM with UV irradiation (365 nm) from the top.

phosphate-buffered saline (PBS, pH = 7.4) and stirred for at least 24 h in darkness, followed by centrifugation and washing extensively with PBS to achieve the drug-loaded AIE-MSNs-CPT (AIE-MSNs-15-CPT or AIE-MSNs-7-CPT) and MSNs-CPT (MSNs-15-CPT or MSNs-7-CPT). The CPT amount in the supernatant and washed solutions was collected and measured using UV–vis spectroscopy at 368 nm to determine the residual CPT content (R_{CPT}, mg). The CPT loading capacity (Q) was evaluated with the loaded CPT mass per gram of AIE-MSNs and later calculated according to the reported equation as follows: Q (mg/g) = (25 − R_{CPT})/0.04.

For drug release assay, 40 mg each of the samples (AIE-MSNs-15-CPT, AIE-MSNs-7-CPT, MSNs-15-CPT, and MSNs-7-CPT) were respectively immersed in PBS (20 mL, pH = 7.4) and incubated in a shaker at 37 °C. At certain time intervals, 3 mL of the supernatant PBS was taken out by centrifugation to test the drug-released concentration by virtue of a UV–vis absorption technique and then returned to the original release media. To better understand their release behavior, the samples were further incubated by constant fresh PBS instead of the tested supernatant to get the release curve. A total of 8 mg of the sample (AIE-MSNs-15-CPT, AIE-MSNs-7-CPT, MSNs-15-CPT, or MSNs-7-CPT) was dispersed into 3 mL of PBS release media, and then the releasing process was performed in the dark at 37 °C. The supernatant was taken out by centrifugation and replaced by another 3 mL of fresh PBS every 2 h. The UV–vis absorbance of the obtained supernatant was measured as well at 368 nm to monitor the CPT release.

3. RESULTS AND DISCUSSION

3.1. Surface Activity of C_{TPE}–C_6–C_{TPE}. The surface activity of C_{TPE}–C_6–C_{TPE} was evaluated through measurement of their surface tension in aqueous solution, which can be employed to evaluate the CMC. As shown in Figure 1a, the surface tension (γ) is plotted against the different concentrations (log C) of C_{TPE}–C_6–C_{TPE}. At low concentration, the surfactant unimers were preferentially adsorbed at the air–

DOI: 10.1021/acs.inorgchem.8b02252
Inorg. Chem. XXXX, XXX, XXX–XXX

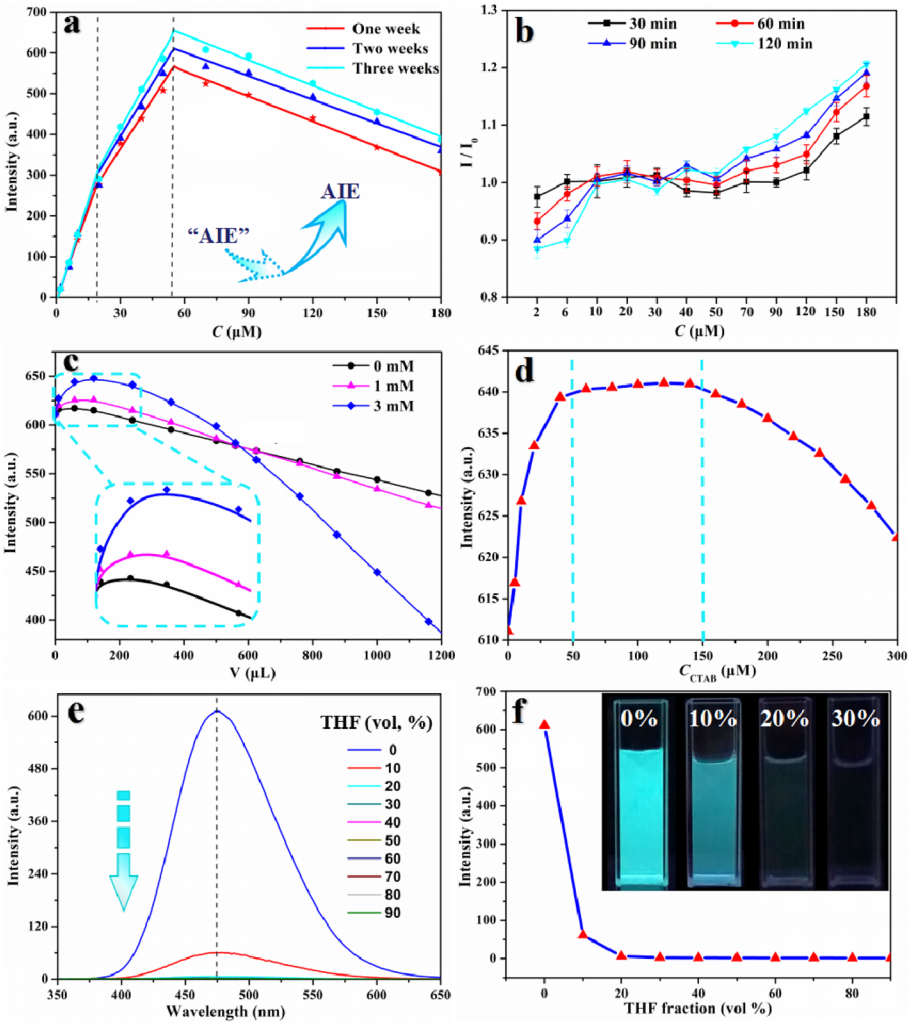

Figure 2. (a) Time-dependent evolution of the fluorescence intensity of C_{TPE}–C_6–C_{TPE} at different concentrations. (b) Photostability of C_{TPE}–C_6–C_{TPE} upon continuous UV excitation at different concentrations. I_0 is the initial fluorescence intensity at 475 nm, and I is the fluorescence intensity of the samples after UV irradiation. (c) Plot of the fluorescence intensity of C_{TPE}–C_6–C_{TPE} (50 μM, 2.5 mL) at 475 nm versus the introducing volume of the CTAB solution with different concentrations. (d) Plot of the fluorescence intensity of C_{TPE}–C_6–C_{TPE} (50 μM) versus the concentration of CTAB in the mixture at a fixed volume. (e) Fluorescence spectra of C_{TPE}–C_6–C_{TPE} in a H_2O/THF mixture (50 μM) with different THF volume fractions (vol: 0–90%). (f) Plot of the fluorescence intensity of C_{TPE}–C_6–C_{TPE} at 475 nm versus the different THF volume fractions in part e. Inset: Photographs of C_{TPE}–C_6–C_{TPE} (50 μM) in a H_2O/THF mixture under 365 nm UV irradiation.

H_2O interface, thus leading to a decrease of the surface tension. In general, the initial adsorption of the surfactant at the air–H_2O interface will reach a saturation state as the concentration continued to increase and then the surface tension came to a balance state accompanied by the formation of micelles. However, because of the strong hydrophobicity and possible π–π stacking of the TPE moieties, C_{TPE}–C_6–C_{TPE} can be continuously adsorbed at the air–H_2O interface after the break point, resulting in a constant decrease of the surface tension. The CMC of C_{TPE}–C_6–C_{TPE} determined from the inflection point in the surface tension curve is 21 μM, which is much lower than that of CTAB (880 μM).[34] On the other hand, the electrical conductivity method was also performed to determine the CMC value of C_{TPE}–C_6–C_{TPE}. A plot of the conductivity (κ) versus the different concentrations (C) of C_{TPE}–C_6–C_{TPE} is shown in Figure 1b. Initially, the solution conductivity increased linearly with a higher slope at the low concentration. This straight line was observed with a decreased slope when the concentrations of C_{TPE}–C_6–C_{TPE} were above 21 μM, ascribed to the fact that the ionic micelles have less charge per unit mass than their unimers.[35] The breakpoint at 21 μM was considered to be the CMC of C_{TPE}–C_6–C_{TPE} and matched well with that obtained from the surface tension measurement.

3.2. Optical Properties of C_{TPE}–C_6–C_{TPE}. The optical properties of C_{TPE}–C_6–C_{TPE} were investigated by UV–vis absorption and fluorescence spectroscopy. Two characteristic peaks at about 248 and 319 nm were observed in their absorption spectra (Figure S1a), which were assigned to absorption of the phenyl groups and the conjugated TPE.[36,37] Meanwhile, their intensities increased linearly with the concentration of C_{TPE}–C_6–C_{TPE} in the range from 0 to 150 μM (Figure S1b). It was noted that the maximum absorption peak position at 319 nm remained unchanged as the concentration increased, indicating that the conformation of C_{TPE}–C_6–C_{TPE} molecules did not depend on the micelle aggregates like other reported TPE derivatives.[36]

Photoluminescence of C_{TPE}–C_6–C_{TPE} was determined by the restriction degree of intramolecular rotation (RIR) of propeller-shaped phenyl rings, which will block the non-

DOI: 10.1021/acs.inorgchem.8b02252
Inorg. Chem. XXXX, XXX, XXX–XXX

radiative pathway and open up the radiative decay channel.[25] On the basis of the RIR mechanism, the light-up fluorescence behavior of $C_{TPE}-C_6-C_{TPE}$ can be realized effectively in the polar aqueous solution because of their excellent water solubility. The fluorescence emission spectra of different concentrations of $C_{TPE}-C_6-C_{TPE}$ in aqueous solution are shown in Figure 1c. Although their maximum emission peak position remained at 475 nm (typical TPE pattern of light) as the concentration increased, the intensity cannot keep increasing as the concentration increased. As shown in Figure 1d, the fluorescence intensity at 475 nm was plotted versus the corresponding concentration of $C_{TPE}-C_6-C_{TPE}$. Three straight lines with different slopes and two inflection points at 20 and 54 μM were found, suggesting the changing aggregation states of $C_{TPE}-C_6-C_{TPE}$ in an aqueous solution. The fluorescence intensity increased linearly with a higher slope at the low concentration, and then the speed slowed after the first inflection point. The decrease in the slope may be ascribed to combined effects including the weakening of RIR, inner filter effect, and some other uncertain effects.[37] The TPE units may get more freedom in the nonpolar interior of the micelles than the outside aqueous environment. The inner filter effect could also happen if the absorbing molecules were at high concentration, inducing the disproportional increase of the photoluminescence intensity with the concentration. This special inflection point at 20 μM was determined as the CMC of $C_{TPE}-C_6-C_{TPE}$, which matched well with that obtained from the surface tension and conductivity measurement. Moreover, the excitation spectra of $C_{TPE}-C_6-C_{TPE}$ were also recorded below and above the CMC (Figure S2). Remarkable red shifts of the peaks in the excitation wavelength were observed when the concentration increased above the CMC, suggesting that the electron transition could be influenced by the assembled $C_{TPE}-C_6-C_{TPE}$ molecules. In contrast, the absorbance is simply proportional to photoluminescence species in other reported AIE surfactants.[33,37] As the concentration of $C_{TPE}-C_6-C_{TPE}$ further increased above 54 μM, an unusual decrease of the fluorescence intensity was observed. This phenomenon could be attributed to the strong hydrophobicity of the TPE moieties in the aggregated micelles, which can significantly improve their assembled nonpolar interior and then weaken the RIR effect as the concentration continuously increased. These results demonstrate that the TPE luminogens connected at the tails of $C_{TPE}-C_6-C_{TPE}$ were sensitive to the nonpolar environment and their photoluminescence can be fully realized in the individual state.

The light-up bright emission of $C_{TPE}-C_6-C_{TPE}$ can be observed directly by the naked eye from their aqueous solution. Figure 1e shows clear fluorescent photographs of the $C_{TPE}-C_6-C_{TPE}$ aqueous solution with the assistance of a UV lamp (365 nm). The brightness of the aqueous solution enhanced significantly as the concentration increased, and a strong cyan emission can be presented even at the low concentration. Such visible fluorescence signals in a dispersed aqueous solution are typical characteristics of AIE surfactants because of their excellent water solubility accompanied by a strong RIR effect.[36] Additionally, the bright-cyan fluorescence of $C_{TPE}-C_6-C_{TPE}$ can also be clearly observed in their solid powder and even frozen state because of the AIE effect (Figure S3), wherein the intramolecular rotation is suppressed by the adjacent molecules to open up the irradiative transition channel. The simultaneous fluorescent emissions of $C_{TPE}-C_6-C_{TPE}$ in the aqueous solution and solid state are quite different from the conventional ACQ fluorophores and AIEgens (nonemissive in the dissolved/dispersed state).[21,22]

To explore the solution stability of $C_{TPE}-C_6-C_{TPE}$, the time-dependent evolution of their fluorescence intensities at different concentrations was investigated by comparing them with their initial values under the same conditions. As shown in Figure 2a, although their emission decreased significantly in the first week, the fluorescence intensities of $C_{TPE}-C_6-C_{TPE}$ with a concentration of less than CMC remain unchanged and the rest begin to recover slowly in the following weeks. Furthermore, the recovering tendency was closely related with the concentration and particularly remarkable in the high-concentration solutions. The initial decline of the fluorescence intensity could be attributed to the further aggregation of $C_{TPE}-C_6-C_{TPE}$ molecules in the aqueous solution drive by the strong hydrophobicity of TPE luminogens. The closer aggregation can provide more available nonpolar interior to weaken the RIR effect, resulting in the unusual aggregation-impaired emission ("AIE"). However, the overcrowded gathering and $\pi-\pi$ stacking between the TPE moieties would further block and weaken the rotation of the phenyl rings (AIE effect) in return, leading to the recovery of their fluorescence emission. Therefore, photoluminescence of $C_{TPE}-C_6-C_{TPE}$ experienced an initial decrease and then turned to recovery as "AIE" changed to AIE. These results reveal that the $C_{TPE}-C_6-C_{TPE}$ aqueous solutions possess durable fluorescence properties and their photoluminescence can also be realized effectively in the aggregated state.

The photostability of $C_{TPE}-C_6-C_{TPE}$ was also investigated by measuring their fluorescence intensities at various time points upon continuous UV irradiation (Figure 2b). Compared with the conventional luminescent materials, $C_{TPE}-C_6-C_{TPE}$ exhibited a distinctive changing tendency and the fluorescence intensities at different concentrations changed inconsistently under the same conditions. For the low-concentration solution, a certain degree of decline appeared with an increase of the exposure time because of photobleaching. However, no significant change was observed in the following concentration, and the fluorescence intensity of the high-concentration solution enhanced rather than decreased with an increase of the exposure time. This unusual phenomenon may be ascribed to photoisomerization of the TPE units induced by UV irradiation,[24] which can destroy the assembled nonpolar environment and then strengthen the RIR effect for high emission.

3.3. Sensitivity of $C_{TPE}-C_6-C_{TPE}$ to CTAB and Organic Solvents. The buffering capacity of $C_{TPE}-C_6-C_{TPE}$ can be investigated by monitoring their fluorescence intensities under continuous dilution. As shown in Figure 2c, the fluorescence intensity of $C_{TPE}-C_6-C_{TPE}$ experienced a slight increase at first and then decreased linearly with the continued introduction of pure H_2O. The initial enhancement of the fluorescence intensity may be ascribed to the destruction of the assembled nonpolar interior, where the RIR effect that has been weakened in the aggregated micelles was recovered. When the solution was constantly diluted by CTAB (1 mM) instead of H_2O, the promotion proceeded more rapidly and then decreased linearly. When the solution was diluted by a higher concentration of CTAB (3 mM), the amplification of the emission was further strengthened, followed by a dramatic linear decrease in the subsequent changing curve. Such an interesting phenomenon probably arose from the changing roles of CTAB on the TPE units in different stages. When

DOI: 10.1021/acs.inorgchem.8b02252
Inorg. Chem. XXXX, XXX, XXX−XXX

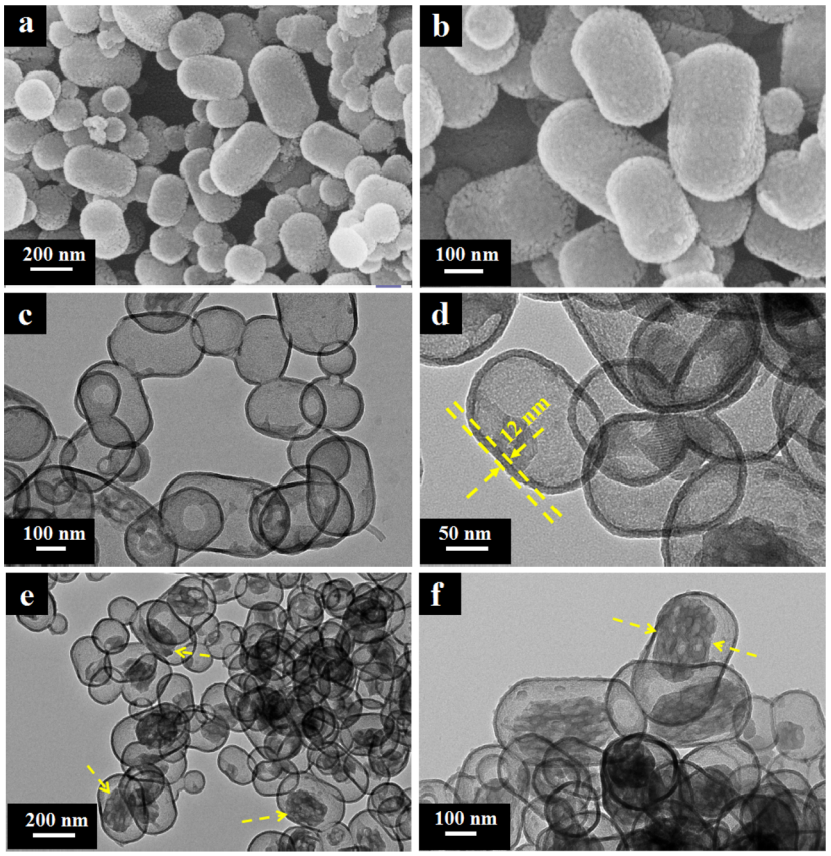

Figure 3. Representative SEM (a and b) and TEM (c and d) images of AIE-SNs-15. TEM images of AIE-SNs-15 with rare rattlelike structures (e and f).

CTAB was introduced at the beginning, the RIR effect could further enhanced by twinning the hydrophobic tails of CTAB with the phenyl rings. Upon continuous dilution with CTAB, the nonpolar environment constructed by excess CTAB could offer freedom instead of the RIR effect for the phenyl rings, leading to distinct effects on the fluorescence intensity. Simultaneously, the binding effects of twinning CTAB can also be observed when $C_{TPE}-C_6-C_{TPE}$ was mixed with CTAB at a fixed volume. As shown in Figure 2d, the fluorescence intensity increased rapidly when CTAB was introduced and then reached a plateau after the concentration reached the same level as that of $C_{TPE}-C_6-C_{TPE}$ (50 μM). With the CTAB concentration continuously increased after 150 μM, the fluorescence intensity began to decrease gradually because of the weakening RIR effect arising from excess CTAB. These results confirm the special sensitivity of $C_{TPE}-C_6-C_{TPE}$ to the nonpolar environment and their intimate relationship with CTAB.

To investigate the sensitivity of $C_{TPE}-C_6-C_{TPE}$ to organic solvents, the fluorescence spectra of $C_{TPE}-C_6-C_{TPE}$ in a H_2O/THF mixture with different THF fractions in volume (vol, 0–90%) were investigated. With increasing THF fractions from 0% to 20% in the THF/H_2O mixture, the fluorescence intensity of $C_{TPE}-C_6-C_{TPE}$ (50 μM) dropped sharply to almost disappear (Figure 2e) and then leveled off as the THF fractions reached 30% (Figure 2f). This "turn-off" phenomenon could also be observed directly by the naked eye, with the solution changing from bright cyan to colorless under 365 nm UV irradiation (inset of Figure 2f). To acquire more detailed information about their sensitivity, $C_{TPE}-C_6-C_{TPE}$ was also dissolved in other organic solvents (acetonitrile, ethanol, and acetone). Only weak signals were observed in their fluorescence spectra (Figure S4). Meanwhile, when ethanol was slowly added to an aqueous solution of $C_{TPE}-C_6-C_{TPE}$, the phase interface could be clearly observed under the bright-cyan fluorescence (Figure S5a). However, this harmonious state and bright fluorescence disappeared immediately after shaking, suggesting that photoluminescence of $C_{TPE}-C_6-C_{TPE}$ was extremely sensitive to organic solvents. In contrast, the phase interface and bright emission could still be found when they mixed with *n*-hexane because of their complete insolubility (Figure S5b).

3.4. Shape-Controlled Preparation of AIE-SNs and Derived AIE-MSNs. The shape-controlled AIE-SNs could be facilely prepared in H_2O via a dual-surfactant-guided one-pot method with CTAB and $C_{TPE}-C_6-C_{TPE}$. As shown in Scheme 1b, $C_{TPE}-C_6-C_{TPE}$ and CTAB were dispersed in H_2O first with continuous stirring to form composite micelles for the facile island nucleation and growth of silica. When TEOS was introduced, the hydrolyzed silicate precursor could be directed to condense into ordered silica structures around micellar templates because of a strong electrostatic interaction.[27] Subsequently, a layer of AIE-SNs formed on the composite micelles via the coassembly of CTAB, $C_{TPE}-C_6-C_{TPE}$, and silicate oligomers, followed by continuous growth and aggregation until the reaction finished. To further understand the role of $C_{TPE}-C_6-C_{TPE}$ in tuning AIE-SNs and their corresponding evolution process, SEM images were used to characterize the products collected under the different molar ratios of CTAB/$C_{TPE}-C_6-C_{TPE}$. As the molar ratio of CTAB/

DOI: 10.1021/acs.inorgchem.8b02252
Inorg. Chem. XXXX, XXX, XXX–XXX

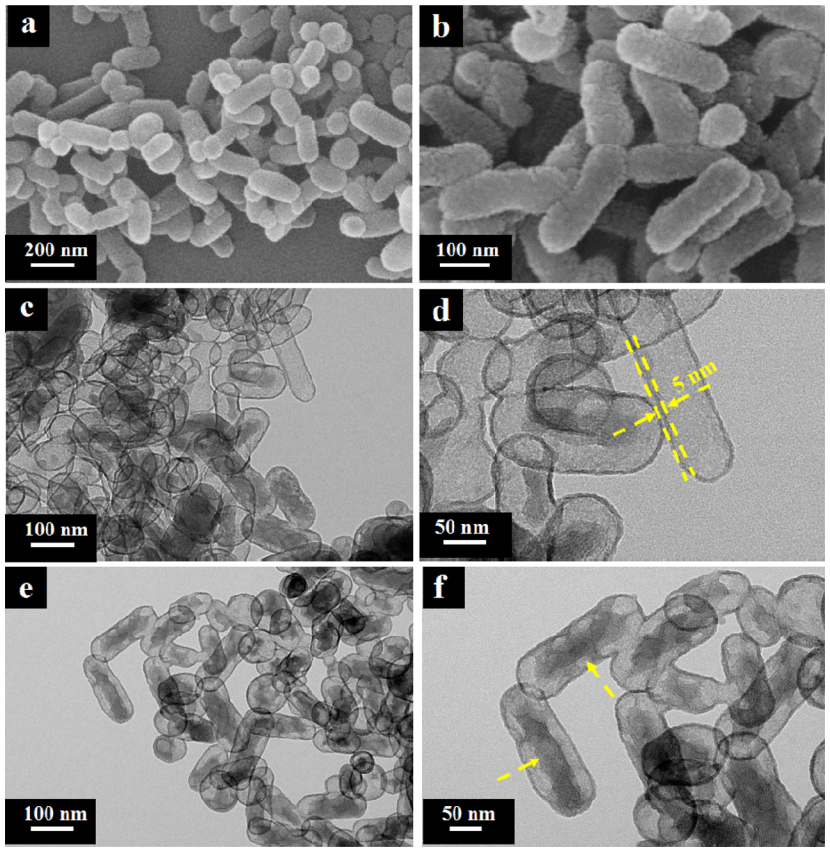

Figure 4. Representative SEM (a and b) and TEM (c and d) images of AIE-SNs-7. TEM images of AIE-SNs-7 with rare rattlelike structures (e and f).

C_{TPE}−C_6−C_{TPE} changed from 40:1 to 5:1, the shapes and sizes of AIE-SNs transformed significantly and the initial irregular aggregates gradually evolved into uniform morphologies (Figure S6). Interestingly, the regular AIE-SNs could further evolve as the molar ratio continuously changed, achieving the shape-controlled preparation of AIE-SNs. At the final molar ratio of 5:1, the AIE-SNs tended to cluster into an elongated rodlike morphology instead of a rounded one (Figure S6i), and some could even reach a length of 800 nm (Figure S7). A summary of the experimental data and processing parameters is given in Table S1, and the products obtained under different molar ratios were denoted as AIE-SNs-*n* (*n* = 40, 35, 30, 25, 20, 15, 10, 7, 5, and 0).

It is noteworthy that two kinds of silica nanorods, AIE-SNs-15 (Figure S6f) and AIE-SNs-7 (Figure S6h), could be prepared directly when the molar ratio of CTAB/C_{TPE}−C_6−C_{TPE} was fixed at 15:1 and 7:1, respectively. As shown in Figure 3a, SEM observation shows that the obtained AIE-SNs-15 have rodlike morphology with a width of ∼200 nm and a length of ∼350 nm. A close observation of AIE-SNs-15 reveals that the nanorods have a relatively coarse surface with tiny cracks (Figure 3b). Furthermore, their internal cavities and shells can also be clearly observed from the high-magnification SEM images of the damaged AIE-SNs-15 obtained under the intense ultrasound (Figure S8). TEM images of AIE-SNs-15 indicate a well-defined hollow structure with an outer shell of a thickness of ∼12 nm (Figure 3c,d). Meanwhile, internal cavities with thin shells are consistent with their external shape. Besides the normal hollow silica nanorods, some rare yolk−shell nanorods with rattle structures, which are difficult to construct by simple methods, appeared in the product (Figures 3e,f and S9). Because of their large void space for cargo storage and delivery, yolk−shell nanomaterials composed of a core within a hollow cavity surrounded by a porous outer shell have been considered to be ideal carriers and nanoreactors.[20]

At a molar ratio of 7:1, the product evolved into uniform narrow silica nanorods in which the width got truncated. As shown in Figure 4a,b, the SEM images of AIE-SNs-7 exhibit rodlike morphology with a width of ∼75 nm and a length of ∼250 nm. The coarse surface with tiny cracks as well as their broken internal cavities and shells can also be clearly observed at a higher magnification (Figure S8). As can be observed from the TEM images of AIE-SNs-7 (Figure 4c,d), the hollow structures can still be found in the product and their shell is much thinner than that of AIE-SNs-15 with a thickness of only ∼5 nm. Compared with the internal structures of AIE-SNs-15, the AIE-SNs-7 was mainly yolk−shell nanorods with rattle structures instead of the normal hollow (Figures 4e,f and S9), indicating that the internal structures of AIE-SNs were also developed along with the external morphology evolution as the molar ratio changed from 15:1 to 7:1.

In addition to the great interest raised by the above products, the observations allow us to partially conceive the roles of C_{TPE}−C_6−C_{TPE} in achieving the tuning of AIE-SNs. The dynamic combined structure-directing effects proposed in our previous research arising from the cooperative CTAB and C_{TPE}−C_6−C_{TPE} can be used to understand their structural evolution process.[33] It is the growing effects of C_{TPE}−C_6−C_{TPE} in the structure-directing process as the molar ratio changes from 40:1 to 5:1 that lead to the continued evolution of the

DOI: 10.1021/acs.inorgchem.8b02252
Inorg. Chem. XXXX, XXX, XXX−XXX

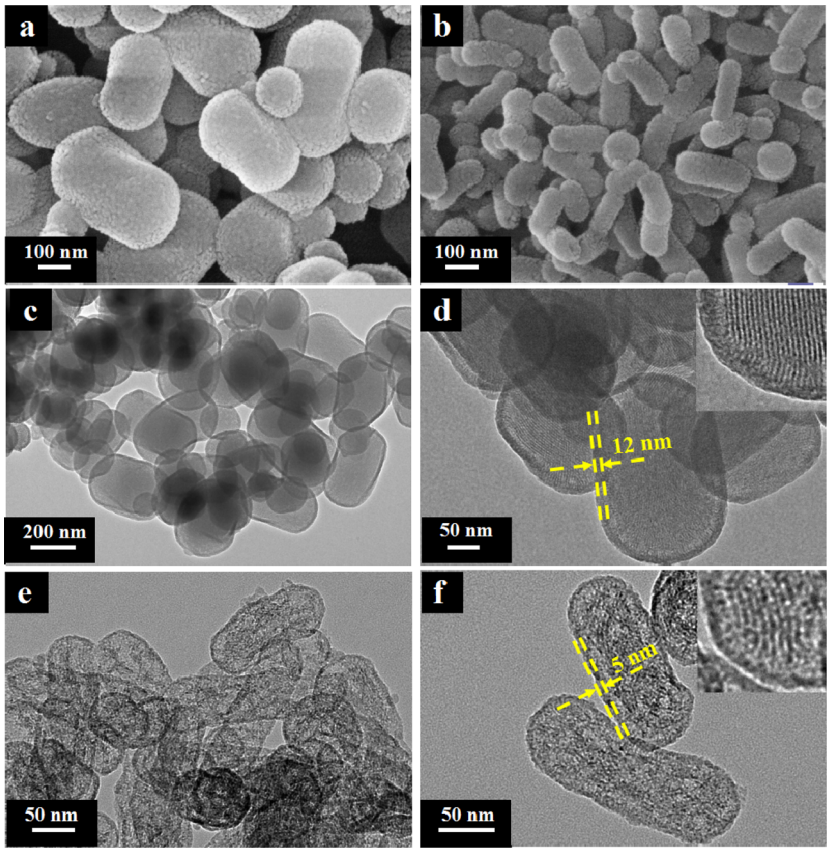

Figure 5. Representative SEM (a) and TEM (c and d) images of AIE-MSNs-15. SEM (b) and TEM (e and f) images of AIE-MSNs-7.

construction. When the amount of $C_{TPE}-C_6-C_{TPE}$ is increased, the effective volume (v) of the hydrophobic group of CTAB/$C_{TPE}-C_6-C_{TPE}$ increases because of the presence of bulky TPE units, which also increases the average packing parameter P of the CTAB/$C_{TPE}-C_6-C_{TPE}$ cosurfactant ($P = v/a_0l_c$, where a_0 is the polar head surface area and l_c is the hydrophobic chain length), resulting in the transformation of the assembled phase.[14] To further understand the structure-directing effect of $C_{TPE}-C_6-C_{TPE}$ in the original system mixed with CTAB, the compared CTAB-SNs were prepared under the direction of the individual CTAB (Figure S10). Meanwhile, AIE-SNs-40, AIE-SNs-30, AIE-SNs-15, and AIE-SNs-5 were also reprepared under the same conditions without the addition of $C_{TPE}-C_6-C_{TPE}$ (Figure S11). Only regular nanospheres could be found in their product, and the nanospheres gradually aggregated into a chaplet shape as the CTAB concentration decreased (Figure S11D). Additionally, it is impossible to obtain a hollow or multifunctional structure with limited CTAB alone according to the literature.[4,19,33] These results show the indispensable role of $C_{TPE}-C_6-C_{TPE}$ in the structure-directing process. On the other hand, CTAB, as a convenient cationic surfactant for building mesoporous silica, was essential for the whole mixed system and acted as the main body in guiding the evolution process of AIE-SNs. Only coralloid AIE-SNs-0 could be obtained under the direction of pure $C_{TPE}-C_6-C_{TPE}$ (Figure S10). All of these results revealed the presence of the combined structure-directing effects of CTAB/$C_{TPE}-C_6-C_{TPE}$ in the preparation of the tuning of AIE-SNs. On the basis of the proposed mechanism, other interesting shapes of AIE-SNs could also be found beyond our research by adjusting the molar ratio properly.

The interaction between the cationic surfactant head groups and anionic silica frame could be broken during the subsequent HCl/ethanol extraction, and then the templating agent was removed from the mesoporous silica.[10] After the coassembly of CTAB, $C_{TPE}-C_6-C_{TPE}$, and silica, the AIE-SNs can transform into AIE-MSNs smoothly by removing the CTAB template. Compared with the simple straight-chain structure of CTAB, it was difficult to remove $C_{TPE}-C_6-C_{TPE}$ from the silica frame because of its complex structure. In particular, the spacer in the gemini surfactant can greatly prevent them from escaping from the rigid structures (Si−O−Si) provided by the silica matrix (Scheme 1b). Therefore, a large amount of $C_{TPE}-C_6-C_{TPE}$ was persistently encapsulated in the silica frame after the removal of CTAB, bringing about both abundant mesoporous and successive fluorescent properties for AIE-MSNs.

SEM and TEM images of AIE-MSNs-15 and AIE-MSNs-7 were investigated to have a better insight of the resultant AIE-MSNs. As shown in Figure 5a,b, AIE-MSNs-15 and AIE-MSNs-7 preserve their original morphologies and display no external differences with AIE-SNs-15 and AIE-SNs-7. The same result can also be found in the SEM images of CTAB-MSNs, AIE-MSNs-30, and AIE-MSNs-5 (Figure S12), revealing the excellent structural stability of AIE-MSNs. According to the TEM images of AIE-MSNs-15 (Figures 5c and S13), it can be seen that silica nanorods have already possessed highly ordered mesoporous channels, wherein the shells and internal hollow cavities can only be ambiguously observed because of the presence of numerous pores. Compared with AIE-SNs-15, the shell thickness of AIE-MSNs-15 showed no obvious change in size and was estimated to be ~12 nm (Figure 5d). Similarly, the indistinct shells and

DOI: 10.1021/acs.inorgchem.8b02252
Inorg. Chem. XXXX, XXX, XXX−XXX

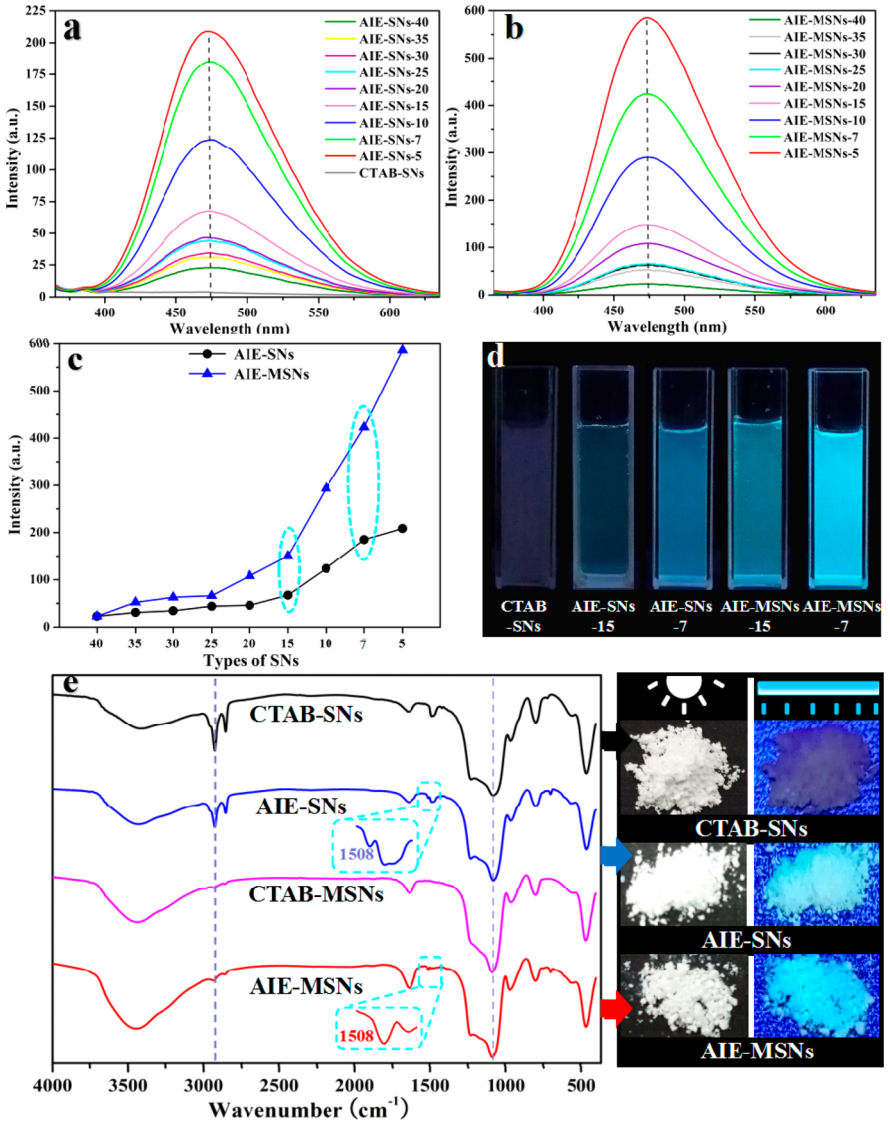

Figure 6. (a) Fluorescence spectra for the different kinds of AIE-SNs and CTAB-SNs (0.25 mg/mL). (b) Fluorescence spectra for the different kinds of AIE-MSNs (0.25 mg/mL). (c) Comparison of the fluorescence intensities for different kinds of AIE-SNs and AIE-MSNs in parts a and b at 475 nm. (d) Fluorescent photographs of CTAB-SNs, AIE-SNs-15, AIE-SNs-7, AIE-MSNs-15, and AIE-MSNs-7 in aqueous dispersion under 365 nm UV irradiation. (e) IR spectra and photographs (taken under room light and 365 nm UV irradiation) of the solid powder of CTAB-SNs, AIE-SNs, CTAB-MSNs, and AIE-MSNs.

internal hollow structures of AIE-MSNs-7 can also be observed in their TEM images (Figures 5e and S13). As shown in Figure 5f, AIE-MSNs-7 exhibited the same shell thickness (~5 nm) as AIE-SNs-7. Compared with the mesoporous silica in AIE-MSNs-15, although AIE-MSNs-7 possessed more noticeable pore structures, their arrangement was inhomogeneous and disordered (insets of Figure 5d,f). Additionally, the original yolk−shell nanorods with rattle structure in AIE-MSNs-15 and AIE-MSNs-7 also became indistinct because of the presence of numerous pores on the shells, suggesting that the CTAB template in AIE-SNs has been effectively removed by the extraction treatment.

3.5. Characterization of AIE-SNs and AIE-MSNs. The fluorescent properties of AIE-SNs and AIE-MSNs were both endowed by the embedded $C_{TPE}-C_6-C_{TPE}$. When the surfactant-directed coassembly was finished, the fluorescence spectra of the residual supernatant solution were investigated after AIE-SNs were removed (Figure S14). Their weak signals suggested that $C_{TPE}-C_6-C_{TPE}$ had been encapsulated into SNs successfully with CTAB. As shown in Figure 6a, the fluorescence intensities for different kinds of AIE-SNs (0.25 mg/mL) were evaluated at the same time. Compared to CTAB-SNs, their fluorescence intensities enhanced, with the types changing from AIE-SNs-40 to AIE-SNs-5. Particularly, the emission (475 nm, Figure S14b) and absorption (319 nm, Figure S15a) wavelengths of AIE-SNs occurred at the same time as the individual $C_{TPE}-C_6-C_{TPE}$ in aqueous solution without a red/blue shift (Figures 1c and S1a), implying that the TPE units in AIE-SNs were free from the restriction of the silica matrix. On the contrary, an obvious shift will be observed if the AIEgens were restricted in the rigid microenvironment provided by the silica matrix.[5,33]

The fluorescence spectra for different kinds of AIE-MSNs with the same concentration (0.25 mg/mL) are shown in Figure 6b. Compared with the original AIE-SNs, AIE-MSNs demonstrated enhanced fluorescence intensities instead of the

DOI: 10.1021/acs.inorgchem.8b02252
Inorg. Chem. XXXX, XXX, XXX−XXX

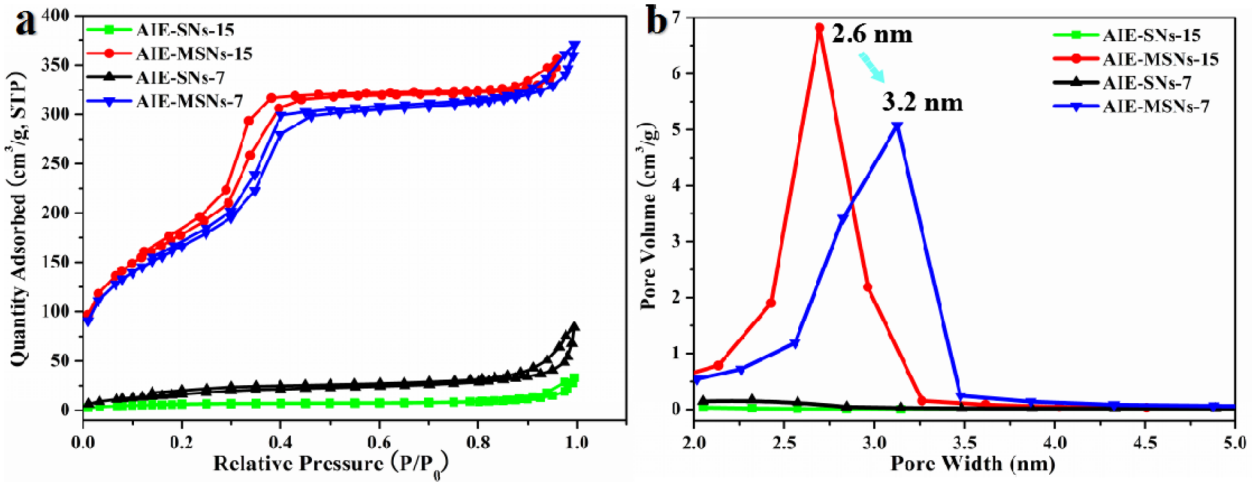

Figure 7. Nitrogen adsorption−desorption isotherms (a) and the corresponding pore size distribution curves (b) of AIE-SNs-15, AIE-MSNs-15, AIE-SNs-7, and AIE-MSNs-7.

traditional weakening caused by the leaking out of fluorescent molecules in the extraction process. As shown in Figure 6c, the remarkable enhancement was recorded with the types of SNs (AIE-SNs-*n* and AIE-MSNs-*n*, where *n* = 40, 35, 30, 25, 20, 15, 10, 7, and 5). Regarding AIE-MSNs-15 and AIE-MSNs-7, their fluorescence intensities were increased up to 2.2- and 2.3-fold, respectively, after the extraction treatment. The improved photoluminescence could also be readily observed by the naked eye in their aqueous dispersion with the assistance of a UV lamp (Figure 6d). The results revealed that the removal of CTAB could bring about not only plenty of mesoporous silica but also outstanding fluorescence emission for the AIE-MSNs. One leading cause for their improved performance is the disappearance of the nonpolar environment constructed by CTAB, which is especially beneficial for photoluminescence of the remaining individual $C_{TPE}-C_6-C_{TPE}$ because of their special sensitivity. Additionally, the presence of a large amount of mesoporous silica in AIE-MSNs caused the anchored $C_{TPE}-C_6-C_{TPE}$ to be fully exposed to H_2O, promoting the RIR effect significantly on the TPE luminogens. The unchanged emission (475 nm, Figure S14b) and absorption (319 nm, Figure S15a) wavelengths of AIE-MSNs compared with AIE-SNs and $C_{TPE}-C_6-C_{TPE}$ further revealed the consistent and unrestricted state of the AIEgens in SNs. A typical Tyndall phenomenon can also be observed in AIE-SNs-15, AIE-SNs-7, AIE-MSNs-15, and AIE-MSNs-7 (Figure S15b), confirming their excellent dispersibility in an aqueous dispersion. Furthermore, the AIE-MSNs possess good photostability, and the fluorescence intensities remained above 70% after 60 min of UV irradiation (Figure S16a). The stability for different types of AIE-MSNs could also be determined by recording the time-dependent evolution of the fluorescence intensity. Their emission decreased after 1 week because of the spontaneous aggregation of AIE-MSNs in aqueous dispersion (Figure S16b). However, further aggregation of AIE-MSNs can induce the strengthening of the AIE effect, leading to the recovery of their fluorescence intensities. The superior fluorescence properties of AIE-MSNs indicate their promising prospects in biomedical applications.

IR spectra of CTAB-SNs, AIE-SNs, CTAB-MSNs, and AIE-MSNs are given in Figure 6e. Compared with CTAB-SNs and AIE-SNs, the stretching vibration bands of CTAB located at 2925, 2856, and 1487 cm^{-1} disappeared in CTAB-MSNs and AIE-MSNs, suggesting that CTAB has been removed successfully by the extraction process.[33] With regard to the incorporated $C_{TPE}-C_6-C_{TPE}$, the characteristic signal located at 1508 cm^{-1} assigned to the stretching vibration of TPE (Figure S3) could be observed in both AIE-SNs and AIE-MSNs, revealing the constant presence of $C_{TPE}-C_6-C_{TPE}$. The results are consistent with the high porosity and successive fluorescence observed in AIE-MSNs. On the other hand, the bright-cyan fluorescence could also be observed in the solid powder of AIE-SNs and AIE-MSNs because of the AIE effect. As shown in Figure 6e, the solid powders of CTAB-SNs, AIE-SNs, and AIE-MSNs are white in appearance under normal room lighting, but strong cyan light can be emitted from AIE-SNs and AIE-MSNs under 365 nm UV irradiation.

Nitrogen adsorption−desorption isotherms of AIE-SNs-15, AIE-MSNs-15, AIE-SNs-7, and AIE-MSNs-7 were recorded to investigate the change of the surface area and porosity before and after removal of the CTAB template (Table S2). As shown in Figure 7a, all of the samples exhibited the combination of type II and IV isotherms with a H4-type hysteresis loop, which was nearly parallel over an appreciable range of relative pressure according to the IUPAC classification.[38] Moreover, a sharply increased nitrogen adsorption plot was observed in the high relative pressure range of 0.8−1.0, which is mainly attributed to the internal voids formed by the randomly distributed and packed SNs. The BET surface areas of AIE-SNs-15 and AIE-SNs-7 were calculated to be only 21.9 and 62.7 m^2/g, respectively. In contrast, the BET surface areas were calculated to be 652.6 and 606.6 m^2/g for AIE-MSNs-15 and AIE-MSNs-7, respectively, which were much larger than those of the unextracted AIE-SNs-15 and AIE-SNs-7. The greatly increased surface areas of AIE-MSNs-15 and AIE-MSNs-7 were consistent with the porous features observed from their TEM images (Figures 5 and S13), and their surface areas were comparable in value with many other hollow MSNs reported in the literature.[14,15,26]

In the synthetic process of MSNs, the length and volume of the hydrophobic alkyl chain of the surfactants can indicate their pore diameter and volume.[28] The pore volumes of AIE-SNs-15 and AIE-SNs-7 were calculated to be 0.047 and 0.127 cm^3/g, while the pore volumes of AIE-MSNs-15 and AIE-MSNs-7 were calculated to be 0.614 and 0.634 cm^3/g, respectively. Because of the presence of more $C_{TPE}-C_6-C_{TPE}$, the pore volume of AIE-SNs-7 has always been larger

DOI: 10.1021/acs.inorgchem.8b02252
Inorg. Chem. XXXX, XXX, XXX−XXX

than that of AIE-SNs-15 before and after the removal of CTAB. In particular, as shown in Figure 7b, AIE-MSNs-7 exhibited larger holes with the pore size center around 3.2 nm. Comparatively, the pore sizes of AIE-MSNs-15 and most reported MSNs are limited to less than 3.0 nm because of the low molecular weight of CTAB.[10,29] Because $C_{TPE}-C_6-C_{TPE}$ contains the bulky TPE luminogens connecting at the tails, the large hydrophobic TPE groups help to organize the micelles, having an empty volume at the center, and are responsible for the larger pore size of AIE-MSNs-7. On the basis of the aforementioned observations, the potential pore size and volume can also be effectively improved by tuning the molar ratio of CTAB/$C_{TPE}-C_6-C_{TPE}$ in the coassembled process. By taking advantage of the bulky TPE groups of $C_{TPE}-C_6-C_{TPE}$, the modified AIE-MSNs with simple operation, high surface areas, and larger pore volumes and sizes would be favorable and promising for further applications in host−guest interaction.

3.6. Drug Loading and Release Behaviors of AIE-MSNs. It is well-known that many anticancer drugs are aromatic and hydrophobic, resulting in poor water solubility and restricted clinical application.[8] The anchored $C_{TPE}-C_6-C_{TPE}$ in AIE-MSNs can provide not only fluorophore but also available hydrophobic TPE units for aromatic drug loading. To confirm their effectiveness in loading the hydrophobic drug, CPT was used as the model guest molecule, and the loading capacities of AIE-MSNs-15 and AIE-MSNs-7 were evaluated as 344.71 and 319.22 mg/g, respectively, which are much higher than those of calcined MSNs-15 (231.12 mg/g) and MSNs-7 (218.54 mg/g). Although the morphologies and frames of MSNs-15 and MSNs-7 were preserved well (Figure S17), the original $C_{TPE}-C_6-C_{TPE}$ was absent in calcined MSNs, resulting in the disappearance of TPE units and corresponding fluorescent properties. The data suggest that AIE-MSNs are superior to calcined MSNs in loading hydrophobic anticancer drugs because of the presence of additional hydrophobic interaction and $\pi-\pi$ stacking. Additionally, an obvious peak of CPT (438 nm) was observed in the fluorescence spectra of AIE-MSNs-CPT because of the covering of a large amount of CPT (Figure S18a), suggesting their good performance in CPT loading.

The in vitro release profiles of CPT from AIE-MSNs-CPT and MSNs-CPT are shown in Figure 8. The release values of AIE-MSNs-CPT are higher than those of MSNs-CPT because of the larger loading capacities of CPT. Meanwhile, AIE-MSNs-15-CPT and AIE-MSNs-7-CPT exhibited similar sustained release curves and drug release reached a plateau after 72 h. However, the amount of CPT released from AIE-MSNs-7-CPT was higher than that of AIE-MSNs-15-CPT at the beginning, although their loading capacity was not outstanding, which may be due to the presence of the larger pore size of AIE-MSNs-7. The same result can also be clearly observed in the release curves of MSNs-15-CPT and MSNs-7-CPT. To better understand their behavior of drug release, AIE-MSNs-CPT and MSNs-CPT were further investigated by constant incubation with fresh PBS instead of the tested supernatant and monitored every 2 h (Figure S18b). The sustained release can be well realized, and CPT can be continuously released for more than 90 h. Meanwhile, the adsorbed CPT can be easily released from AIE-MSNs-7-CPT and MSNs-7-CPT because of their advantageous pore size, resulting in the larger release amount at the beginning than that of AIE-MSNs-15-CPT and MSNs-15-CPT. In addition, the release curves were both up and down accompanied by several releasing upsurges instead of a constant decrease as the time goes on, which strongly suggested their complex internal structures.

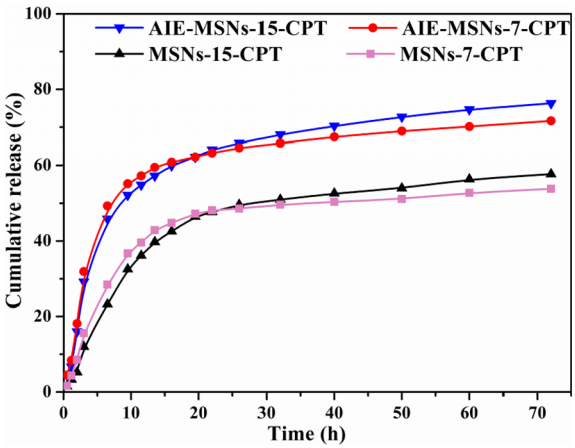

Figure 8. In vitro cumulative release profiles of CPT from AIE-MSNs-15-CPT, AIE-MSNs-7-CPT, MSNs-15-CPT, and MSNs-7-CPT.

4. CONCLUSIONS

In summary, a TPE-functionalized gemini surfactant $C_{TPE}-C_6-C_{TPE}$ was designed and synthesized to develop a straightforward method for the controllable preparation of hollow AIE-MSNs. The versatile $C_{TPE}-C_6-C_{TPE}$ possesses superior water solubility, surface activity, stability, and sensitivity to CTAB and organic solvents and can realize photoluminescence simultaneously in dispersed, aggregated, and solid states. In the preparation of tunable AIE-SNs, $C_{TPE}-C_6-C_{TPE}$ will not only provide an anchored fluorophore but also serve as an intimate partner of CTAB to regulate their construction. By proper tuning of the molar ratio of CTAB/$C_{TPE}-C_6-C_{TPE}$, the morphologies of AIE-SNs could be tuned effectively and two kinds of silica nanorods (AIE-SNs-15 and AIE-SNs-7) were produced directly. After the extraction of CTAB, AIE-SNs can evolve into AIE-MSNs successfully and bring about abundant mesoporous silica and high accessible surface area. It is noteworthy that the incorporated bulky TPE luminogens can not only provide enhanced fluorescence for AIE-MSNs to overcome the inevitable weakening of the fluorescence intensity caused by leakage but also improve their internal structure, endowing AIE-MSNs-7 with larger pore size (3.2 nm) and pore volume (0.634 cm^3/g). Moreover, the resultant AIE-MSNs-15 and AIE-MSNs-7 can both serve as the desired nanocarriers of the hydrophobic anticancer drug for their high loading capacities and long release times. The proposed $C_{TPE}-C_6-C_{TPE}$ enriches the family of gemini surfactants and opens new perspectives to controllably prepare advanced fluorescent mesoporous materials with simple operation for the future large-scale industrial production and various applications in bioimaging, drug delivery, bioenrichment and separation, sensing, and so on.

■ ASSOCIATED CONTENT

Supporting Information

The Supporting Information is available free of charge on the ACS Publications website at DOI: 10.1021/acs.inorgchem.8b02252.

DOI: 10.1021/acs.inorgchem.8b02252
Inorg. Chem. XXXX, XXX, XXX−XXX

Supplementary figures and tables regarding the synthesis, characterization of $C_{TPE}-C_6-C_{TPE}$, AIE-SNs, and AIE-MSNs, and other experiments (PDF)

AUTHOR INFORMATION

Corresponding Author

*E-mail: gzn@whu.edu.cn.

ORCID

Zhinong Gao: 0000-0003-2855-5334

Author Contributions

The manuscript was written through contributions of all authors.

Notes

The authors declare no competing financial interest.

ACKNOWLEDGMENTS

This work was supported by the Fundamental Research Funds for the Chinese Central Universities (Grant 2012203020211).

REFERENCES

(1) Wang, F.; Xiao, J.; Chen, S.; Sun, H.; Yang, B.; Jiang, J.; Zhou, X.; Du, J. Polymer Vesicles: Modular Platforms for Cancer Theranostics. *Adv. Mater.* **2018**, *30*, 1705674−1705681.

(2) Wang, H.; Chen, Q.; Zhou, S. Carbon-Based Hybrid Nanogels: A Synergistic Nanoplatform for Combined Biosensing, Bioimaging, and Responsive Drug Delivery. *Chem. Soc. Rev.* **2018**, *47*, 4198−4232.

(3) Xing, P.; Zhao, Y. Supramolecular Vesicles for Stimulus-Responsive Drug delivery. *Small Methods* **2018**, *2*, 1700364−1700379.

(4) Zhang, X.; Zhang, X.; Wang, S.; Liu, M.; Zhang, Y.; Tao, L.; Wei, Y. Facile Incorporation of Aggregation-Induced Emission Materials into Mesoporous Silica Nanoparticles for Intracellular Imaging and Cancer Therapy. *ACS Appl. Mater. Interfaces* **2013**, *5*, 1943−1947.

(5) Wang, Y.-F.; Che, J.; Zheng, Y.-C.; Zhao, Y.-Y.; Chen, F.; Jin, S.-B.; Gong, N.-Q.; Xu, J.; Hu, Z.-B.; Liang, X.-J. Multi-Stable Fluorescent Silica Nanoparticles Obtained from in Situ Doping with Aggregation-Induced Emission Molecules. *J. Mater. Chem. B* **2015**, *3*, 8775−8781.

(6) Croissant, J. G.; Fatieiev, Y.; Almalik, A.; Khashab, N. M. Mesoporous Silica and Organosilica Nanoparticles: Physical Chemistry, Biosafety, Delivery Strategies, and Biomedical Applications. *Adv. Healthcare Mater.* **2018**, *7*, 1700831−1700905.

(7) Yan, S.; Hu, F.; Hong, X.; Shuai, Q. Water-Soluble Ferrocene Complexes (WFCs) Functionalized Silica Nanospheres for WFC Delivery in HepG2 Tumor Therapy. *Mater. Sci. Eng., C* **2018**, *90*, 397−406.

(8) Li, N.; Niu, D.; Jiang, Y.; Xu, C.; Pan, S.; He, J.; Chen, J.; Zhang, L.; Li, Y. Morphology Evolution and Spatially Selective Functionalization of Hierarchically Porous Silica Nanospheres for Improved Multidrug Delivery. *Chem. Mater.* **2017**, *29*, 10377−10385.

(9) He, Q.; Shi, J.; Chen, F.; Zhu, M.; Zhang, L. An Anticancer Drug Delivery System Based on Surfactant-Templated Mesoporous Silica Nanoparticles. *Biomaterials* **2010**, *31*, 3335−3346.

(10) Coti, K. K.; Belowich, M. E.; Liong, M.; Ambrogio, M. W.; Lau, Y. A.; Khatib, H. A.; Zink, J. I.; Khashab, N. M.; Stoddart, J. F. Mechanised Nanoparticles for Drug Delivery. *Nanoscale* **2009**, *1*, 16−39.

(11) Xuan, M.; Shao, J.; Zhao, J.; Li, Q.; Dai, L.; Li, J. Magnetic Mesoporous Silica Nanoparticles Cloaked by Red Blood Cell Membranes: Applications in Cancer Therapy. *Angew. Chem., Int. Ed.* **2018**, *57*, 6049−6053.

(12) Zhu, Y.; Shi, J.; Shen, W.; Dong, X.; Feng, J.; Ruan, M.; Li, Y. Stimuli-Responsive Controlled Drug Release from a Hollow Mesoporous Silica Sphere/Polyelectrolyte Multilayer Core-Shell Structure. *Angew. Chem.* **2005**, *117*, 5213−5217.

(13) Yeh, Y. Q.; Chen, B. C.; Lin, H. P.; Tang, C. Y. Synthesis of Hollow Silica Spheres with Mesostructured Shell Using Cationic-Anionic-Neutral Block Copolymer Ternary Surfactants. *Langmuir* **2006**, *22*, 6−9.

(14) Zhang, Y.; Zhou, G.; Sun, B.; Zhao, M.; Zhang, J.; Chen, F. A Cationic-Cationic Co-Surfactant Templating Route for Synthesizing Well-Defined Multilamellar Vesicular Silica with an Adjustable Number of Layers. *Chem. Commun.* **2014**, *50*, 2907−2909.

(15) Yang, Y.; Yu, M.; Song, H.; Wang, Y.; Yu, C. Preparation of Fluorescent Mesoporous Hollow Silica-Fullerene Nanoparticles Via Selective Etching for Combined Chemotherapy and Photodynamic Therapy. *Nanoscale* **2015**, *7*, 11894−11898.

(16) Li, L.; Tang, F.; Liu, H.; Liu, T.; Hao, N.; Chen, D.; Teng, X.; He, J. In Vivo Delivery of Silica Nanorattle Encapsulated Docetaxel for Liver Cancer Therapy with Low Toxicity and High Efficacy. *ACS Nano* **2010**, *4*, 6874−6882.

(17) Wang, S.; Chen, M.; Wu, L. One-Step Synthesis of Cagelike Hollow Silica Spheres with Large through-Holes for Macromolecule Delivery. *ACS Appl. Mater. Interfaces* **2016**, *8*, 33316−33325.

(18) Chiu, H.-Y.; Gößl, D.; Haddick, L.; Engelke, H.; Bein, T. Clickable Multifunctional Large-Pore Mesoporous Silica Nanoparticles as Nanocarriers. *Chem. Mater.* **2018**, *30*, 644−654.

(19) Li, Y.; Li, N.; Pan, W.; Yu, Z.; Yang, L.; Tang, B. Hollow Mesoporous Silica Nanoparticles with Tunable Structures for Controlled Drug Delivery. *ACS Appl. Mater. Interfaces* **2017**, *9*, 2123−2129.

(20) Lin, L. S.; Song, J.; Yang, H. H.; Chen, X. Yolk-Shell Nanostructures: Design, Synthesis, and Biomedical Applications. *Adv. Mater.* **2018**, *30*, 1704639−1704668.

(21) Liang, J.; Tang, B. Z.; Liu, B. Specific Light-up Bioprobes Based on AIEgen Conjugates. *Chem. Soc. Rev.* **2015**, *44*, 2798−2811.

(22) Yan, L.; Zhang, Y.; Xu, B.; Tian, W. Fluorescent Nanoparticles Based on AIE Fluorogens for Bioimaging. *Nanoscale* **2016**, *8*, 2471−2487.

(23) Zhou, Z.; Zhang, C. C.; Zheng, Y.; Wang, Q. Aggregation Induced Emission Mediated Controlled Release by Using a Built-in Functionalized Nanocluster with Theranostic Features. *J. Med. Chem.* **2016**, *59*, 410−418.

(24) Fang, X.; Zhang, Y.-M.; Chang, K.; Liu, Z.; Su, X.; Chen, H.; Zhang, S. X.-A.; Liu, Y.; Wu, C. Facile Synthesis, Macroscopic Separation, E/Z Isomerization, and Distinct AIE Properties of Pure Stereoisomers of an Oxetane-Substituted Tetraphenylethene Luminogen. *Chem. Mater.* **2016**, *28*, 6628−6636.

(25) Li, D.; Yu, J. AIEgens-Functionalized Inorganic-Organic Hybrid Materials: Fabrications and Applications. *Small* **2016**, *12*, 6478−6494.

(26) Fan, Z.; Li, D.; Yu, X.; Zhang, Y.; Cai, Y.; Jin, J.; Yu, J. AIE Luminogen-Functionalized Hollow Mesoporous Silica Nanospheres for Drug Delivery and Cell Imaging. *Chem. - Eur. J.* **2016**, *22*, 3681−3685.

(27) Kresge, C. T.; Leonowicz, M. E.; Roth, W. J.; Vartuli, J. C.; Beck, J. S. Ordered Mesoporous Molecular Sieves Synthesized by a Liquid-Crystal Template Mechanism. *Nature* **1992**, *359*, 710−712.

(28) Kim, J.; Kim, B.; Anand, C.; Mano, A.; Zaidi, J. S.; Ariga, K.; You, J.; Vinu, A.; Kim, E. A Single-Step Synthesis of Electroactive Mesoporous Prodot-Silica Structures. *Angew. Chem., Int. Ed.* **2015**, *54*, 8407−8410.

(29) Zhang, Y.; Yue, Q.; Yu, L.; Yang, X.; Hou, X.; Zhao, D.; Cheng, X.; Deng, Y. Amphiphilic Block Copolymers Directed Interface Coassembly to Construct Multifunctional Microspheres with Magnetic Core and Monolayer Mesoporous Aluminosilicate Shell. *Adv. Mater.* **2018**, *30*, 1800345−1800354.

(30) Liao, X.; Gao, Z.; Xia, Y.; Niu, F.; Zhai, W. Rational Design and Synthesis of Carboxylate Gemini Surfactants with an Excellent Aggregate Behavior for Nano-La2o3Morphology-Controllable Preparation. *Langmuir* **2017**, *33*, 3304−3310.

(31) Xia, Y.; Gao, Z.; Liao, X.; Pan, C.; Zhang, Y.; Feng, X. Rapid Synthesis of Hierarchical, Flower-Like Ag Microstructures with a Gemini Surfactant as a Directing Agent for SERS Applications. *CrystEngComm* **2017**, *19*, 6547−6555.

(32) Yan, S.; Wei, W.; Gao, Z.; Xia, Y.; Han, J. Gemini Surfactant with Pyrrolidinium Head Groups and a Hydroxyl-Substituted Spacer:

DOI: 10.1021/acs.inorgchem.8b02252
Inorg. Chem. XXXX, XXX, XXX−XXX

Surface Properties and Assisted One-Pot Synthesis of Dendritic Au Nanocrystals. *New J. Chem.* **2018**, *42*, 11573−11582.
(33) Yan, S.; Gao, Z.; Xia, Y.; Liao, X.; Han, J.; Pan, C.; Zhang, Y.; Zhai, W. Aggregation-Induced Emission Gemini Surfactant-Assisted Fabrication of Shape-Controlled Fluorescent Hollow Mesoporous Silica Nanoparticles. *Eur. J. Inorg. Chem.* **2018**, *2018*, 1891−1901.
(34) Yatcilla, M. T.; Herrington, K. L.; Laura, L.; Brasher, a.; Kaler, E. W.; Chiruvolu, S.; Zasadzinski, J. A. Phase Behavior of Aqueous Mixtures of Cetyltrimethylammonium Bromide (CTAB) and Sodium Octyl Sulfate (SOS). *J. Phys. Chem.* **1996**, *100*, 5874−5879.
(35) Shi, L.; Lundberg, D.; Musaev, D. G.; Menger, F. M. [12]Annulene Gemini Surfactants: Structure and Self-Assembly. *Angew. Chem., Int. Ed.* **2007**, *46*, 5889−5891.
(36) Guan, W.; Zhou, W.; Lu, C.; Tang, B. Z. Synthesis and Design of Aggregation-Induced Emission Surfactants: Direct Observation of Micelle Transitions and Microemulsion Droplets. *Angew. Chem., Int. Ed.* **2015**, *54*, 15160−15164.
(37) Guan, W.; Wang, S.; Lu, C.; Tang, B. Z. Fluorescence Microscopy as an Alternative to Electron Microscopy for Microscale Dispersion Evaluation of Organic-Inorganic Composites. *Nat. Commun.* **2016**, *7*, 11811−11817.
(38) Sing, K. S. W. Reporting Physisorption Data for Gas/Solid Systems-with Special Reference to the Determination of Surface Area and Porosity. *Pure Appl. Chem.* **1985**, *57*, 603−619.

DOI: 10.1021/acs.inorgchem.8b02252
Inorg. Chem. XXXX, XXX, XXX−XXX